Published in final edited form as:
Magn Reson Med. 2018 January ; 79(1): 317–326. doi:10.1002/mrm.26684.

Estimating breast tumor blood flow during neoadjuvant chemotherapy using interleaved high temporal and high spatial resolution MRI

Dr Leonidas Georgiou, PhD,
Division of Biomedical Imaging, University of Leeds, Leeds, UK

Dr Nisha Sharma, MB, MRCP, FRCR,
Department of Radiology, Leeds Teaching Hospital NHS Trust, Leeds, UK

Mr David A Broadbent, MSc, BA,
Department of Medical Physics and Engineering, Leeds Teaching Hospital NHS Trust, Leeds, UK; Division of Biomedical Imaging, University of Leeds, Leeds, UK

Dr Daniel J. Wilson, PhD,
Department of Medical Physics and Engineering, Leeds Teaching Hospital NHS Trust, Leeds, UK

Dr Barbara J Dall, MB, FRCR,
Department of Radiology, Leeds Teaching Hospital NHS Trust, Leeds, UK

Dr Anmol Gangi, MBChB, BSc, and
Department of Western General Hospital, NHS Lothian, Edinburgh, UK; Division of Biomedical Imaging, University of Leeds, Leeds, UK

Prof David L. Buckley, PhD
Division of Biomedical Imaging, University of Leeds, Leeds, UK

Abstract

Purpose—To evaluate an interleaved MRI sampling strategy that acquires both high temporal resolution (HTR) dynamic contrast-enhanced (DCE) data for quantifying breast tumor blood flow (TBF) and high spatial resolution (HSR) DCE data for clinical reporting, following a single standard injection of contrast agent.

Methods—A simulation study was used to evaluate the performance of the interleaved technique under different conditions. In a prospective clinical study, eighteen patients with primary breast cancer due to undergo NACT, were examined using interleaved HTR and HSR DCE-MRI at 1.5T. Tumor regions of interest (ROI) were analyzed with a two-compartment tracer kinetic model. Paired parameters (n=10) from data acquired before and post-cycle 2 of NACT were compared using the nonparametric Wilcoxon signed-rank test.

Results—Simulations demonstrated that TBF was reliably estimated using the proposed strategy. ROI analysis revealed significant changes in TBF (0.81 to 0.43 ml/min/ml; P=0.002) following 2

Corresponding Author: David L. Buckley, PhD, Division of Biomedical Imaging, University of Leeds, Clarendon Way, Leeds, LS2 9JT, UK. d.l.buckley@leeds.ac.uk; tel. +44 113 343 2017.

Europe PMC Funders Author Manuscripts

cycles of NACT. HSR data were reported in the normal way and enabled the assessment of tumor volume, which decreased by 53% following NACT (P=0.065).

Conclusion—TBF can be measured reliably using the proposed strategy without compromising a standard clinical protocol. Furthermore, in our feasibility study TBF decreased significantly following NACT whereas capillary permeability surface-area product did not.

Keywords

DCE-MRI; tracer kinetic model; breast; tumor blood flow; chemotherapy; high temporal resolution

Introduction

Breast cancer is the most common cancer in women worldwide. Survival rates for women who are diagnosed early have improved, but this is not the case with late stage disease (1). Patients with advanced breast cancer often undergo neoadjuvant chemotherapy (NACT), with the aim of reducing tumor size. Nevertheless a significant proportion of patients do not benefit from the treatment (2), but still suffer from its side effects (3,4). It is important to identify these patients at an early stage of treatment and, where possible, change their therapy.

Treatment response is currently assessed by a combination of clinical examination and imaging techniques such as mammography, ultrasound and MRI. However, these techniques are typically limited to evaluating morphological changes, such as tumor diameter (5) and volume (6). It is recognized that changes in physiology, such as tumor blood flow (TBF), precede morphological changes and this allows an assessment of treatment response at an earlier stage of therapy (7,8). Since 1990 several studies have demonstrated that it is possible to estimate physiological processes using dynamic contrast enhanced (DCE)-MRI and many studies have exploited this approach to monitor NACT response, either by semi-quantitative signal-time curve characterization or by measurement and modeling of tumor contrast uptake (9–13).

Despite the promise of DCE-MRI to monitor treatment response, there has been limited adoption of quantitative MRI techniques into clinical practice. Accurate modeling of tracer kinetic time series requires the use of imaging protocols with high temporal resolution (HTR) and such data are usually acquired at the expense of high spatial resolution (HSR) (14). The American College of Radiology guidelines recommend the acquisition of HSR data: a slice thickness of less than 3 mm with in-plane spatial resolution of 1 mm (or less), suggesting that a temporal resolution of less than 4 minutes will suffice for “accurate capture of lesion kinetics” (http://www.acr.org/Quality-Safety/Standards-Guidelines). In the case of TBF measurement however, the sampling interval plays a major role with the necessity of acquiring data in both the breasts and a feeding artery (15–17). A sampling rate of 1 imaging volume every 2 or 3 s is needed to capture the temporal characteristics of the arterial input function (AIF) during the early passes of the contrast agent bolus though this sampling rate can be relaxed later in the time-course (16,17).

Europe PMC Funders Author Manuscripts

Some studies simply neglect HSR images or breast coverage to improve the sampling rate (14,18,19) while others have proposed different approaches to meet these conflicting requirements. A two-bolus technique was proposed to allow for separate HSR and HTR imaging however it significantly increases scanning time and reduces the contrast dose that can be used in each bolus (20). Song et al demonstrated a technique that allows acquisition of HTR images (12–15 s) while simultaneously allowing the reconstruction of HSR images from the same datasets (21). Saranathan et al proposed an acquisition technique that switched between HTR with moderate spatial resolution (9 s; 1.1×2.5×4 mm) during the contrast agent wash-in phase and low temporal resolution but HSR (120 s; 1.1×1×1.2 mm) during the wash-out phase (22). Despite these proposals, acquisition rates for estimation of TBF remain suboptimal (16,17).

An alternative approach to that of Saranathan et al. is to acquire HSR and HTR images in an interleaved manner. The use of a dual-echo multi-slice acquisition by Grovik et al (23) hampered measurement of the AIF but enabled DCE-MRI at HTR while retaining HSR images for clinical use. The purpose of this study is to evaluate the feasibility of quantifying tumor blood flow (TBF) in patients with advanced breast cancer undergoing neoadjuvant chemotherapy (NACT), using an interleaved dynamic contrast-enhanced (DCE) MR imaging technique.

Methods

Tracer kinetic model and sampling requirements

A two-compartment exchange model (2CXM) describes the transport of contrast agent through a tumor in terms of TBF (F_b), capillary permeability surface-area product (PS), blood volume fraction (v_b) and extracellular extravascular space (EES) volume fraction (v_e). The following time-domain solution was used for analysis of the signal-time data:

$$C(t) = F_b(1 - Hct) \cdot C_p(t) \otimes \left[A \cdot e^{-\alpha t} + (1 - A) \cdot e^{-\beta t}\right] \quad [1]$$

where, $C_p(t)$ is the AIF, the blood plasma concentration of contrast agent, C(t) is the concentration in the tumor and ⊗ is the convolution symbol (15,24). The fit parameters (F_b, A, α and β) can be used to derive the required tracer kinetic parameters as follows

$$\begin{aligned} v_b &= F_b/(A \cdot (\alpha - \beta) + \beta), \\ PS &= (1 - Hct) \cdot \left[v_b\left(\alpha + \beta - \alpha\beta v_b/F_b\right) - F_b\right], \\ v_e &= PS \,.\, F_b/\left(\alpha\beta v_b\right), \quad E = PS/\left[PS + F_b \cdot (1 - Hct)\right], \\ K^{trans} &= E \cdot F_b \cdot (1 - Hct) \end{aligned} \quad [2]$$

where Hct is the large vessel hematocrit, E is the extraction fraction and K^{trans} is the volume transfer constant. Quantitative analysis requires a signal from the tumor and the lumen of a feeding artery (the AIF). The proposed interleaved imaging scheme (Fig. 1) starts by

Europe PMC Funders Author Manuscripts

acquiring a HSR volume that serves as a baseline reference for clinical reporting. During contrast agent administration, the acquisition scheme continues with HTR sampling to capture the rapid changes of the AIF and tissue curve during the early bolus passes. The acquisition then alternates between HSR and HTR for a further 6 minutes.

Simulations

In order to evaluate the performance of the interleaved strategy, a simulation study was undertaken. A realistic AIF (25) was simulated at HTR (0.1 s) and convolved with the tissue model given in Eq. 1 (using model and acquisition parameters presented in Table 1) to generate 3 typical tumor curve types – 3, 4 & 5 (26).

The HTR relative signal intensity (RSI) time curves generated were regridded to match the temporal resolution of our proposed MR technique (2.2 s). Tumor curves and the AIF were further processed to include random Gaussian noise at four different signal-to-noise ratios (SNR) of 20, 30, 50 and 80. SNR was defined as the maximum signal intensity in the time series divided by the standard deviation of the baseline signal (27,28). 1000 tissue curves were generated for each of the tumor curve types at each SNR level.

The time series were cropped to simulate three sampling strategies (see Fig. 1); method 1- continuous HTR imaging for approximately 8 minutes, method 2 - as method 1 with gaps for HSR imaging as in the clinical protocol and method 3 - as method 2 with the initial burst of HTR data shortened (method 2: 36 volumes, method 3: 21 volumes) to remove the second pass of the AIF and simulate a protocol which allows earlier HSR acquisition.

Patients

Eighteen female patients (mean age, 48.7 years) who had locally advanced breast cancer, due to undergo NACT and have been referred for an MRI scan for treatment assessment, were eligible to this prospective study and imaged at least twice during their course of NACT. The study was approved by a research ethics committee and written informed consent was obtained. Blood samples from each patient were used to estimate the large vessel Hct before each MRI scan. Patients with contraindications to MRI were excluded from the study. Table 2 shows the histological and molecular markers acquired from core sample biopsies obtained at baseline and the subsequent NACT regimen for each patient.

MR imaging

All patients were scanned on a 1.5 T Avanto MR scanner (Siemens, Erlangen, Germany), positioned head first prone, using a bilateral breast coil for signal reception. To enhance signal from the descending aorta (which was used for the AIF (14) as there is no local artery of sufficient diameter that can be reliably measured in the imaging volume) a flexible matrix coil was also positioned on the patients' back.

The clinical protocol began with a T_1-weighted 3D spoiled gradient echo (FLASH) and a T_2-weighted turbo spin echo (TSE) sequence each in the transverse plane covering both breasts. Following this, axial images (FOV: 340×340×150 mm, reconstruction matrix: 128×128×30) were acquired using a 3D inversion recovery (IR) prepared balanced steady

state free precession sequence (TrueFISP) at four inversion times (TI: 400, 680, 1200 and 2000 ms) to measure the baseline T_1 relaxation times of blood and tumor (IR-TR: 3000 ms, TR/TE: 2.7/1.3 ms, FA: 70°, GRAPPA parallel factor: 2, T_{acq}: 1 min per volume).

For HTR and HSR DCE-MRI, standard vendor-supplied 3D FLASH sequences were employed. No modification was made to the HSR DCE-MRI images used in our institution for clinical reporting. These were preset to run in an interleaved manner as illustrated in Fig. 1. The system was setup to traverse through the sequences in an automated mode, without reshimming or re-tuning procedures in-between. For the HTR imaging the same geometry as the T_1 mapping was used (TR/TE: 2.7/0.8 ms, FA: 21°, GRAPPA factor 2, T_{acq} = 2.2 s). For the HSR images a 3D fat-suppressed FLASH sequence was used to generate axial images (TR/TE: 4.1/1.2 ms, FA: 10°, FOV: 340×340×146 mm, reconstruction matrix size: 384×384×104, GRAPPA factor: 2, T_{acq} = 34 s). A dose of 0.1 mmol/kg Gd-DOTA (Dotarem, Guerbet Laboratories, Aulnays Sous Bois, France) was administered at 3 ml/s followed by 20 ml saline at the start of HTR imaging. The total acquisition time of the dynamic data was approximately 8 minutes during which 84 HTR volumes and 8 HSR volumes were acquired.

Postprocessing

All MRI data were processed using PMI (Platform for Research in Medical Imaging, version 0.4 (29)) and Matlab (Mathworks, Nattick, MA, USA). The IR images were used to obtain baseline $T_{1,0}$ relaxation time maps by fitting Eq. 2 to the signal intensity data using a non-linear least-squares optimization algorithm, on a voxel-by-voxel basis

$$S = S_0\left(1 - 2 \cdot e^{-TI/T_{1,0}}\right) \quad [3]$$

where S_0 is the steady state signal. PMI was used to draw ROIs in the descending aorta and tumor in order to obtain the AIF and the corresponding tumor curve. For AIF selection, ROIs that covered several slices within the 3D volume of HTR data for each patient were first created. The 3D ROIs were then trimmed to include only voxels that had a maximum RSI value between 50 and 95% of all RSI maxima (chosen empirically). A 2nd criterion for AIF selection was that voxels were only included if the corresponding $T_{1,0}$ estimates were within 1.1 and 1.7 s. These steps were followed to minimize potential errors in the AIF such as partial volume, inflow or motion artifacts. The median number of voxels included in the AIF ROI was 426 (range 105 – 576).

Tumor 3D ROIs were selected on both HSR and HTR images. For the HSR data, a radiologist examined all MRI datasets (T_1 and T_2-weighted volumes as well as the postcontrast dynamic data) and delineated the tumor. Both enhancing and non-enhancing areas within the tumor were selected and these ROIs were used for tumor volume estimation. The 3D ROIs for the HTR images only included regions that exhibited contrast enhancement.

The RSI data were converted to longitudinal relaxation rate changes (ΔR_1) using the mean precontrast $T_{1,0}$ estimate and the signal intensity obtained with a FLASH sequence (Eq. 3)

$$S = S_0 \cdot \left(\frac{1 - e^{-TR/T_1}}{1 - \cos(FA) \cdot e^{-TR/T_1}} \right) . \sin(FA) \cdot e^{-TE/T_2^*} \quad [4]$$

where S_0 is proportional to the proton density and given the short TE used, the term $\exp(-TE/T_2^*)$ was assumed to remain unchanged at a value of 1 throughout. The resulting time series were subsequently used for tracer kinetic modeling. The model was initially fitted with five parameters, the four parameters defined in Eq. 1 and bolus arrival time (BAT) that accounts for the delay between arrival of the contrast at the aorta and the tumor. A second fit was performed with BAT fixed at its best-fit value. The analysis was performed in Matlab using a constrained non-linear least-squares optimization algorithm (F_b, A, α and β were constrained to be positive and A<1). To fill the gaps in the AIF left by the acquisition of HSR data, interpolation was achieved using a best-fit decaying bi-exponential function (30). The analysis was performed blinded to any clinical results.

To compare $T_{1,0}$, tumor volume and tracer kinetic parameter estimates before and following treatment (for paired data only, n=10), a non-parametric Wilcoxon signed rank test was used, since the parameter estimates were not normally distributed (Shapiro-Wilk test, p>0.05). In addition, Spearman's rank correlation coefficient was used to assess the relationship between parameters (for paired data only). For the analysis of the simulated data, percentage error was calculated for each parameter

$$Percentage\ Error = \frac{x - x_{true}}{x_{true}} \times 100\% \quad [4]$$

where x and x_{true} are the estimated and the simulated value of the parameter.

Results

Simulations

Simulated data for all three curve types at four SNR levels were fitted and parameter estimates were generated. Due to the large quantity of data generated in the simulations (3 curve types, 4 SNR levels and 4 estimated parameters per fit), we only present the results for a SNR of 50 (Fig. 2), which is closest to the mean SNR calculated from the subsequent MRI experiments.

The most reliable parameter estimate was F_b. Fig. 2 demonstrates that all three sampling strategies generate similar median estimates for F_b. However, interquartile range (IQR) in F_b estimates was narrowest for method 1, wider for method 2 and widest for method 3. Furthermore, IQR of F_b estimates for all sampling strategies becomes larger as the curve type changed from type 3 to type 5. Similar effects were observed for both PS and v_b

estimates. In contrast, v_e estimates showed a larger IQR for type 3 and 5 curves compared to type 4. The results for the remaining SNR levels followed similar trends, but the IQR of the parameter estimates increased as SNR decreased.

Scatter plots for combinations of parameter estimates (Figs. 3&4) illustrate that some fit errors occurred with type 3 and 5 curves. In general, these failures become more frequent as SNR decreased and as the number of data points used to fit the data decreased. Fig. 3 demonstrates the low precision in v_e estimates for type 3 curves at a SNR of 20, and how this improved at a SNR of 50 and as more data points were used in the fitting process (i.e. methods 1 and 2 outperform method 3).

Fig. 4 (bottom row) shows that fitting a type 5 curve acquired with sampling method 3 and, to a lesser extent, with method 2, leads to fit failures. In particular, 2% and 27% of the fits generate a PS estimate close to 0 for method 2 and method 3, respectively and the number of fits failures increased as SNR decreased. The inability to estimate PS from these data leads to arbitrary v_e estimates, an overestimation of v_b and an underestimation of F_b. The corresponding scatter plots for type 4 curves (Fig.4, top row) indicate that the distribution of the parameter estimates is more homogeneous, without fit errors and with the parameter estimates confined to a narrower range.

Clinical application

In this cross-sectional feasibility study we analyzed 25 MRI data sets from 15 of the 18 patients recruited; those 15 had baseline MRI scans and 10 of them went on to have MRI scans following 2 cycles of EC. Three patients have missed their baseline scan due to a lack of scanner availability at the time and were excluded from the study. Five patients missed their post-cycle 2 MRI scan due to technical failures or variations in oncology requests for MRI. At surgery following the completion of NACT, 3 of these 10 patients (patient no. 1, 3 and 14) showed a complete pathological response and 7 showed evidence of partial pathological response.

Examples of the HSR and HTR images acquired are shown in Figs. 5 and 6, along with the corresponding signal-time curves. Example model fits for patients at baseline and post-cycle 2 are illustrated in Fig. 7. Median values and ranges of the resulting parameter estimates are shown in Table 3. There was a significant change between baseline and post-cycle 2 in F_b, BAT and K^{trans} estimates at the 95% confidence level (P = 0.002, 0.020 and 0.037, respectively). There were no significant changes in the remaining parameters. Tumor volume, determined from the HSR data, decreased by 53% following 2 cycles of NACT but this change was not significant at the 95% confidence level (P = 0.065).

K^{trans} (calculated as $E \cdot F_b \cdot (1\text{-Hct})$) correlated better with PS ($\rho = 0.94$, $p<0.001$) than with F_b ($\rho = 0.69$, P = 0.011) and shows a borderline significant change in response to treatment compared to F_b. Conversely if, as is common, a one compartment model (1CM) is used to estimate K^{trans} (though an F-test suggests that the 2CXM model is preferred14; data not shown), it correlates strongly with F_b ($\rho = 0.94$, $P<0.001$), weakly with PS ($\rho = 0.47$, P = 0.037) and shows a more significant reduction following NACT (32%, P = 0.010).

Discussion

In this study, we have evaluated the performance of the interleaved acquisition strategy introduced in Fig. 1. The protocol was compared to a conventional HTR protocol in the absence of interleaving through simulations and clinical feasibility was subsequently tested through application in patients undergoing NACT.

Simulations

The performance of the proposed interleaved strategy (sampling method 2) was comparable to method 1 (HTR without gaps). The IQR of the parameter estimates varied with curve type but improved as SNR increased. F_b was the parameter that could be estimated with the highest accuracy and precision, irrespective of curve type or SNR.

Simulations using sampling method 1 revealed the sources of error expected when a continuous HTR series is acquired. For type 3 curves, all parameter estimates (except v_e) are confined to a narrow range. When PS is low (type 3) there is slow contrast agent extravasation and the curve continues to rise. The overall acquisition time is suboptimal for this curve type with insufficient time for contrast agent to fill the EES. This leads to difficulties in estimating v_e and an uptake model may be more appropriate (15). Nevertheless, the accuracy and precision of v_e estimates improves as SNR increases (Fig. 3).

The performance of the proposed interleaved acquisition strategy (method 2) was comparable to method 1 in most cases. Similar characteristics were observed for type 3 curves, but v_e estimates were more variable. The main difference between the two methods was observed in fitting type 5 curves. Here extravasation (PS) is high, and makes it difficult to differentiate contrast agent in the vascular and EES compartments. This may lead to imprecise PS, v_e and v_b estimates, worsening as the SNR and number of points used to sample the time series decrease. In the limit $PS \rightarrow \infty$, the model collapses to a 1CM, where the estimate of blood plasma volume fraction (v_p) is equal to $v_e + v_p$, and v_e no longer has an impact on the curve and can take any value as seen in ~2% of the fits at SNR 50. The number of fit errors reduces as the SNR increases.

Sampling method 3 was evaluated through simulations in order to examine the importance of acquiring all rapid temporal changes of the AIF during the first minutes of dynamic acquisition. The results of the simulation suggest that reducing the number of data points can have a significant impact on the parameter estimates. Method 3 generated a higher number of imprecise v_e estimates in the case of type 3 curves. Moreover the percentage of fits that result in fit failure in type 5 curves was appreciably higher (27% of fits for an SNR of 50, increasing as SNR decreases).

Based on the simulations we concluded that the proposed interleaved acquisition scheme was able to generate sufficiently reliable parameter estimates compared to those obtained with a conventional HTR protocol. It appears to be important to sample all the early signal changes in the AIF.

Europe PMC Funders Author Manuscripts

Clinical application

The acquisition technique proposed offers the potential to derive separate estimates for TBF and PS, and at the same time maintain the acquisition of HSR data necessary for clinical reporting. Since the basic structure of the routine protocol was maintained (other than a delayed acquisition of the first post-contrast HSR volume), our radiologists were able to follow the normal breast MRI reporting system (31). Figs. 5 and 6 show examples of type 5 and type 4 curves with data from the HSR images which match the kinetic curve type derived from the HTR images.

Our estimates of baseline tumor and blood T_1 using the inversion recovery sequence are in the range of previous results (19,32–34). To our knowledge, only Brix et al. previously provided F_b estimates for breast tumors using DCE-MRI techniques and these compare well with our F_b estimates for untreated tumors (regional blood flow: ~0.61±0.25 ml/min/ml (14)). There is also good agreement between v_b estimates (0.25±0.10), whereas v_e reported by Brix (0.34±0.16) is somewhat higher than our median estimate. In other studies using PET and O-15 labeled water, whole tumor mean F_b estimates in breast tumors range from 30-60 ml/min/100 g (8,35–37) but may be systematically underestimated due to limitations in spatio-temporal resolution.

We measured a significant reduction (47%, $P = 0.002$) in median F_b following 2 cycles of NACT (n=10). A similar reduction following NACT was also reported using PET imaging by Mankoff et al[7]. K^{trans} has been used in previous MRI studies to monitor treatment response but this parameter is often measured in different ways and misinterpreted (38). The physiological interpretation of K^{trans} reflects a combination of TBF and PS (15). However the contribution of each process, and hence the sensitivity of the analysis is likely to be dependent on model selection. These findings in conjunction with our simulations suggest that F_b is a good choice for measuring treatment induced changes.

Limitations

Although 18 patients were initially recruited only 10 had both baseline and post-cycle 2 MRI scans. Within the study cohort patients were treated with a variety of NACT regimens and this complicates any attempt to derive a correlation between TBF change and pathological response.

Although the first segment of HTR data was prolonged in order to capture the rapid temporal changes in the blood concentration of contrast agent during the first minutes following administration, there were examples of AIF time series with visible first, second and third passes before the acquisition switched. This should have minimal effect on F_b estimates, but may, in some cases, have an impact on PS and v_b estimates. Furthermore, a better sampling strategy for the HTR images could further improve the accuracy and precision of parameter estimates in general. Additional simulations (data not shown) demonstrated that more frequent but shorter sampling intervals could improve these metrics.

It is important to note that a 2CXM is a gross-simplification of the true distribution of contrast media in breast cancers. For example a study has shown that contrast media accumulate within the ducts, 2 minutes post-contrast administration (39). Nevertheless, the

application of complex models is not always the best approach since this depends on several requirements such as noise in the time series, temporal sampling rate, accuracy of AIF measurement (40). In this study the data did not support a model with more than 4 parameters.

Conclusions

To our knowledge this is the first study that presents an acquisition strategy to acquire both HSR images for clinical reporting and HTR images for quantitative DCE-MRI, with the ability to derive separate estimates of TBF and PS. The interleaved approach was evaluated using simulation studies and tested through application in patients undergoing NACT. These techniques will allow radiologists to adapt similar protocol strategies without significantly compromising the data used for clinical reporting and encourage other investigators to examine the physiological characteristics of tumors and their associated changes during treatment.

Acknowledgements

Preliminary findings from this study were presented at the ISMRM 20th Annual Meeting in Melbourne in 2012. The study was funded, in part, by Breast Cancer Now (award 2014MayPR241). The authors wish to thank Trish Snowden for her hard work in patient recruitment and MRI scanning.

References

1. Institute NC. [Accessed: March 20, 2017] SEER Cancer Statistics Factsheets: Female Breast Cancer. Available at:https://seer.cancer.gov/statfacts/html/breast.html
2. Makris A, Powles TJ, Ashley SE, Chang J, Hickish T, Tidy VA, Nash AG, Ford HT. Original article A reduction in the requirements for mastectomy in a randomized trial of neoadjuvant chemoendocrine therapy in primary breast cancer. Annals of Oncology. 1998:1179–1184. [PubMed: 9862047]
3. Reinisch M, von Minckwitz G, Harbeck N, Janni W, Kümmel S, Kaufmann M, Elling D, Nekljudova V, Loibl S. Side effects of standard adjuvant and neoadjuvant chemotherapy regimens according to age groups in primary breast cancer. Breast care (Basel, Switzerland). 2013; 8:60–6.
4. Shapiro CL, Recht A. Side effects of adjuvant treatment of breast cancer. The New England journal of medicine. 2001; 344:1997–2008. [PubMed: 11430330]
5. Eisenhauer EA, Therasse P, Bogaerts J, Schwartz LH, Sargent D, Ford R, Dancey J, Arbuck S, Gwyther S, Mooney M, et al. New response evaluation criteria in solid tumours: Revised RECIST guideline (version 1.1). European Journal of Cancer. 2009; 45:228–247. [PubMed: 19097774]
6. Hylton NM, Gatsonis CA, Rosen MA, Lehman CD, Newitt DC, Partridge SC, Bernreuter WK, Pisano ED, Morris EA, Weatherall PT, et al. Neoadjuvant Chemotherapy for Breast Cancer: Functional Tumor Volume by MR Imaging Predicts Recurrence-free Survival-Results from the ACRIN 6657/CALGB 150007 I-SPY 1 TRIAL. Radiology. 2015; 000:150013.
7. Wasser K, Klein SK, Fink C, Junkermann H, Sinn HP, Zuna I, Knopp MV, Delorme S. Evaluation of neoadjuvant chemotherapeutic response of breast cancer using dynamic MRI with high temporal resolution. European radiology. 2003; 13:80–87. [PubMed: 12541113]
8. Mankoff, Da; Dunnwald, LK; Gralow, JR; Ellis, GK; Schubert, EK; Tseng, J; Lawton, TJ; Linden, HM; Livingston, RB. Changes in blood flow and metabolism in locally advanced breast cancer treated with neoadjuvant chemotherapy. Journal of nuclear medicine : official publication, Society of Nuclear Medicine. 2003; 44:1806–1814.
9. Bone B, Szabo BK, Perbeck LG, Veress B, Aspelin P. Can contrast-enhanced MR imaging predict survival in breast cancer? Acta Radiol. 2003; 44:373–378. [PubMed: 12846686]

10. Ah-See M-LW, Makris a, Taylor NJ, Harrison M, Richman PI, Burcombe RJ, Stirling JJ, d'Arcy Ja, Collins DJ, Pittam MR, et al. Early Changes in Functional Dynamic Magnetic Resonance Imaging Predict for Pathologic Response to Neoadjuvant Chemotherapy in Primary Breast Cancer. Clinical Cancer Research. 2008; 14:6580–6589. [PubMed: 18927299]
11. Pickles MD, Manton DJ, Lowry M, Turnbull LW. Prognostic value of pre-treatment DCE-MRI parameters in predicting disease free and overall survival for breast cancer patients undergoing neoadjuvant chemotherapy. European Journal of Radiology. 2009; 71:498–505. [PubMed: 18572340]
12. Padhani AR, Khan AA. Diffusion-weighted (DW) and dynamic contrast-enhanced (DCE) magnetic resonance imaging (MRI) for monitoring anticancer therapy. Targeted oncology. 2010; 5:39–52. [PubMed: 20383784]
13. Li, Sonia P; Makris, Andreas; Beresford, Mark J; Taylor, N Jane; Ah-See, Mei-Lin W; Stirling, J James; d'Arcy, James A; Collins, David J; Kozarski, Robert; Padhani, Anwar R. Use of Dynamic Contrast-enhanced MR Imaging to Predict Survival in Patients with Primary Breast Cancer Undergoing Neoadjuvant Chemotherapy. Radiology. 2011; 260:68–78. [PubMed: 21502383]
14. Brix G, Kiessling F, Lucht R, Darai S, Wasser K, Delorme S, Griebel J. Microcirculation and microvasculature in breast tumors: pharmacokinetic analysis of dynamic MR image series. Magnetic resonance in medicine. 2004; 52:420–9. [PubMed: 15282828]
15. Sourbron SP, Buckley DL. Tracer kinetic modelling in MRI: estimating perfusion and capillary permeability. Physics in medicine and biology. 2012; 57:R1–33. [PubMed: 22173205]
16. Henderson E, Rutt BK, Lee TY. Temporal sampling requirements for the tracer kinetics modeling of breast disease. Magnetic Resonance Imaging. 1998; 16:1057–1073. [PubMed: 9839990]
17. Luypaert R, Sourbron S, de Mey J. Validity of perfusion parameters obtained using the modified Tofts model: a simulation study. Magnetic resonance in medicine. 2011; 65:1491–7. [PubMed: 21500273]
18. Mussurakis S, Buckley DL, Drew PJ, Fox JN, Carleton PJ, Turnbull LW, Horsman A. Dynamic MR imaging of the breast combined with analysis of contrast agent kinetics in the differentiation of primary breast tumours. Clinical Radiology. 1997; 52:516–526. [PubMed: 9240704]
19. Delille J-P, Slanetz PJ, Yeh ED, Halpern EF, Kopans DB, Garrido L. Invasive ductal breast carcinoma response to neoadjuvant chemotherapy: noninvasive monitoring with functional MR imaging pilot study. Radiology. 2003; 228:63–9. [PubMed: 12775851]
20. Makkat S, Luypaert R, Sourbron S, Stadnik T, De Mey J. Quantification of perfusion and permeability in breast tumors with a deconvolution-based analysis of second-bolus T1-DCE data. Journal of Magnetic Resonance Imaging. 2007; 25:1159–1167. [PubMed: 17520720]
21. Song HK, Dougherty L, Schnall MD. Simultaneous acquisition of multiple resolution images for dynamic contrast enhanced imaging of the breast. Magnetic Resonance in Medicine. 2001; 46:503–509. [PubMed: 11550242]
22. Saranathan M, Rettmann DW, Hargreaves BA, Lipson JA, Daniel BL. Variable spatiotemporal resolution three-dimensional Dixon sequence for rapid dynamic contrast-enhanced breast MRI. Journal of Magnetic Resonance Imaging. 2014; 40:1392–1399. [PubMed: 24227703]
23. Grøvik E, Bjørnerud A, Storås TH, Gjesdal KI. Split dynamic MRI: Single bolus high spatial-temporal resolution and multi contrast evaluation of breast lesions. Journal of Magnetic Resonance Imaging. 2014; 39:673–682. [PubMed: 23913511]
24. Leach MO, Morgan B, Tofts PS, Buckley DL, Huang W, Horsfield Ma, Chenevert TL, Collins DJ, Jackson a, Lomas D, et al. Imaging vascular function for early stage clinical trials using dynamic contrast-enhanced magnetic resonance imaging. European radiology. 2012; 22:1451–64. [PubMed: 22562143]
25. Parker GJM, Roberts C, Macdonald A, Buonaccorsi GA, Cheung S, Buckley DL, Jackson A, Watson Y, Davies K, Jayson GC. Experimentally-derived functional form for a population-averaged high-temporal-resolution arterial input function for dynamic contrast-enhanced MRI. Magn Reson Med. 2006; 56:993–1000. [PubMed: 17036301]
26. Daniel BL, Yen YF, Glover GH, Ikeda DM, Birdwell RL, Sawyer-Glover AM, Black JW, Plevritis SK, Jeffrey SS, Herfkens RJ. Breast disease: dynamic spiral MR imaging. Radiology. 1998; 209:499–509. [PubMed: 9807580]

27. Calamante F, Gadian DG, Connelly A. Quantification of bolus-tracking MRI: Improved characterization of the tissue residue function using Tikhonov regularization. Magnetic resonance in medicine : official journal of the Society of Magnetic Resonance in Medicine / Society of Magnetic Resonance in Medicine. 2003; 50:1237–47.
28. Cho GY, Moy L, Zhang JL, Baete S, Lattanzi R, Moccaldi M, Babb JS, Kim S, Sodickson DK, Sigmund EE. Comparison of fitting methods and b-value sampling strategies for intravoxel incoherent motion in breast cancer. Magnetic resonance in medicine. 2015; 74:1077–85. [PubMed: 25302780]
29. Sourbron S, Biffar A, Ingrisch M, Fieren Y, Luypaert R. PMI: Platform for Research in Medical Imaging. Magn Reson Mater Phy. 2009; 22:539.
30. Weinmann HJ, Laniado M, Mützel W. Pharmacokinetics of GdDTPA/dimeglumine after intravenous injection into healthy volunteers. Physiological chemistry and physics and medical NMR. 1984; 16:167–72. [PubMed: 6505043]
31. Morris, EA, Comstock, CE, Lee, CH, Lehman, CD, Ikeda, DM. ACR BI-RADS magnetic resonance imagingACR BI-RADS atlas, breast imaging reporting and data system. Reston, VA: American College of Radiology; 2013. 56–71.
32. Barth M, Moser E. Proton NMR relaxation times of human blood samples at 1.5 T and implications for functional MRI. Cellular and molecular biology (Noisy-le-Grand). 1997; 43:783–91.
33. Roberts C, Little R, Watson Y, Zhao S, Buckley DL, Parker GJM. The effect of blood inflow and B(1)-field inhomogeneity on measurement of the arterial input function in axial 3D spoiled gradient echo dynamic contrast-enhanced MRI. Magnetic resonance in medicine : official journal of the Society of Magnetic Resonance in Medicine / Society of Magnetic Resonance in Medicine. 2011; 65:108–19.
34. Brix G, Zwick S, Kiessling F, Griebel J. Pharmacokinetic analysis of tissue microcirculation using nested models: multimodel inference and parameter identifiability. Medical physics. 2009; 36:2923–33. [PubMed: 19673191]
35. Specht JM, Kurland BF, Montgomery SK, Dunnwald LK, Doot RK, Gralow JR, Ellis GK, Linden HM, Livingston RB, Allison KH, et al. Tumor metabolism and blood flow as assessed by positron emission tomography varies by tumor subtype in locally advanced breast cancer. Clinical cancer research : an official journal of the American Association for Cancer Research. 2010; 16:2803–2810. [PubMed: 20460489]
36. Wilson CBJH, Lammertsma Aa, Mckenzie CG, Sikora K, Jones T. Measurements of Blood Flow and Exchanging Water Space in Breast Tumors Using Positron Emission Tomography : A Rapid and Noninvasive Dynamic Method Measurements of Blood Flow and Exchanging Water Space in Breast Tumors Using Positron Emission Tomography. Cancer research. 1992; 52:1592–1597. [PubMed: 1540969]
37. Hentschel M, Paulus T, Mix M, Moser E, Nitzsche EU, Brink I. Analysis of blood flow and glucose metabolism in mammary carcinomas and normal breast: a H2(15)O PET and 18F-FDG study. Nuclear Medicine Communications. 2007; 28:789–97. [PubMed: 17728609]
38. Sourbron SP, Buckley DL. On the scope and interpretation of the Tofts models for DCE-MRI. Magnetic resonance in medicine : official journal of the Society of Magnetic Resonance in Medicine / Society of Magnetic Resonance in Medicine. 2011; 66:735–45.
39. Jansen SA, Paunesku T, Fan X, Woloschak GE, Vogt S, Conzen SD, Krausz T, Newstead GM, Karczmar GS. Ductal carcinoma in situ: X-ray fluorescence microscopy and dynamic contrast-enhanced MR imaging reveals gadolinium uptake within neoplastic mammary ducts in a murine model. Radiology. 2009; 253:399–406. [PubMed: 19864527]
40. Duan C, Kallehauge JF, Bretthorst GL, Tanderup K, Ackerman JJH, Garbow JR. Are complex DCE-MRI models supported by clinical data? Magn Reson Med. 2017; 77:1329–1339. [PubMed: 26946317]

Europe PMC Funders Author Manuscripts

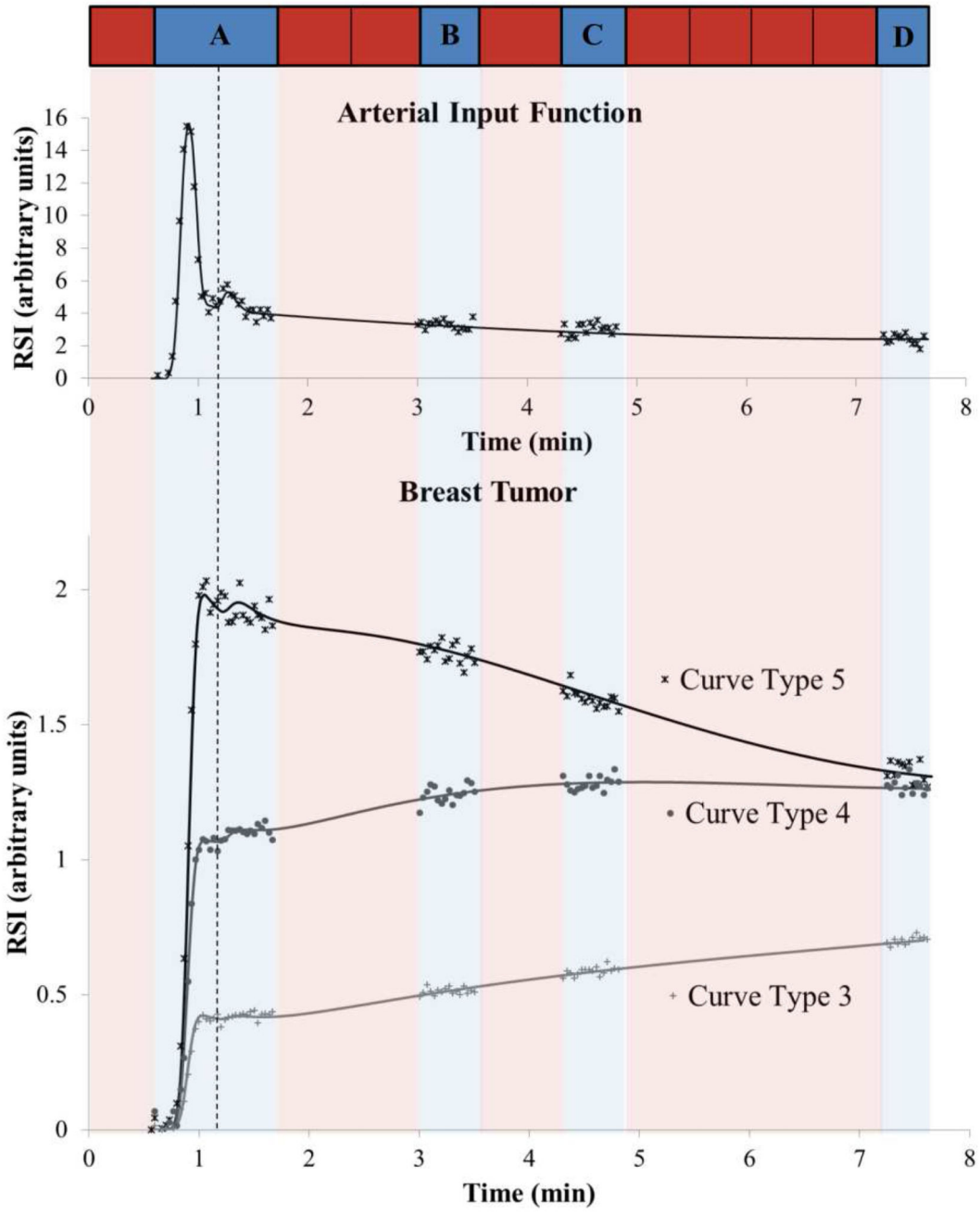

Figure 1.

Schematic of the interleaved acquisition with example simulated AIF and three tumor curve types. The solid lines represent the simulated time series (without gaps or noise) and the marker points illustrate the data acquired with the interleaved technique (with noise). Red and blue segments represent high spatial resolution (HSR) and high temporal resolution (HTR) acquisitions, respectively. At the first burst of HTR imaging (segment A) 36 volumes were acquired for method 2, to encompass the first two passes of the contrast agent bolus. For method 3, this was reduced to 21 volumes (acquisition stops at the dotted line) to

exclude the 2nd pass of the AIF. During the following bursts (segments B, C and D) 16 time points were acquired, each segment occupying the acquisition time of a single HSR volume. There were eight HSR volumes acquired in total.

Europe PMC Funders Author Manuscripts

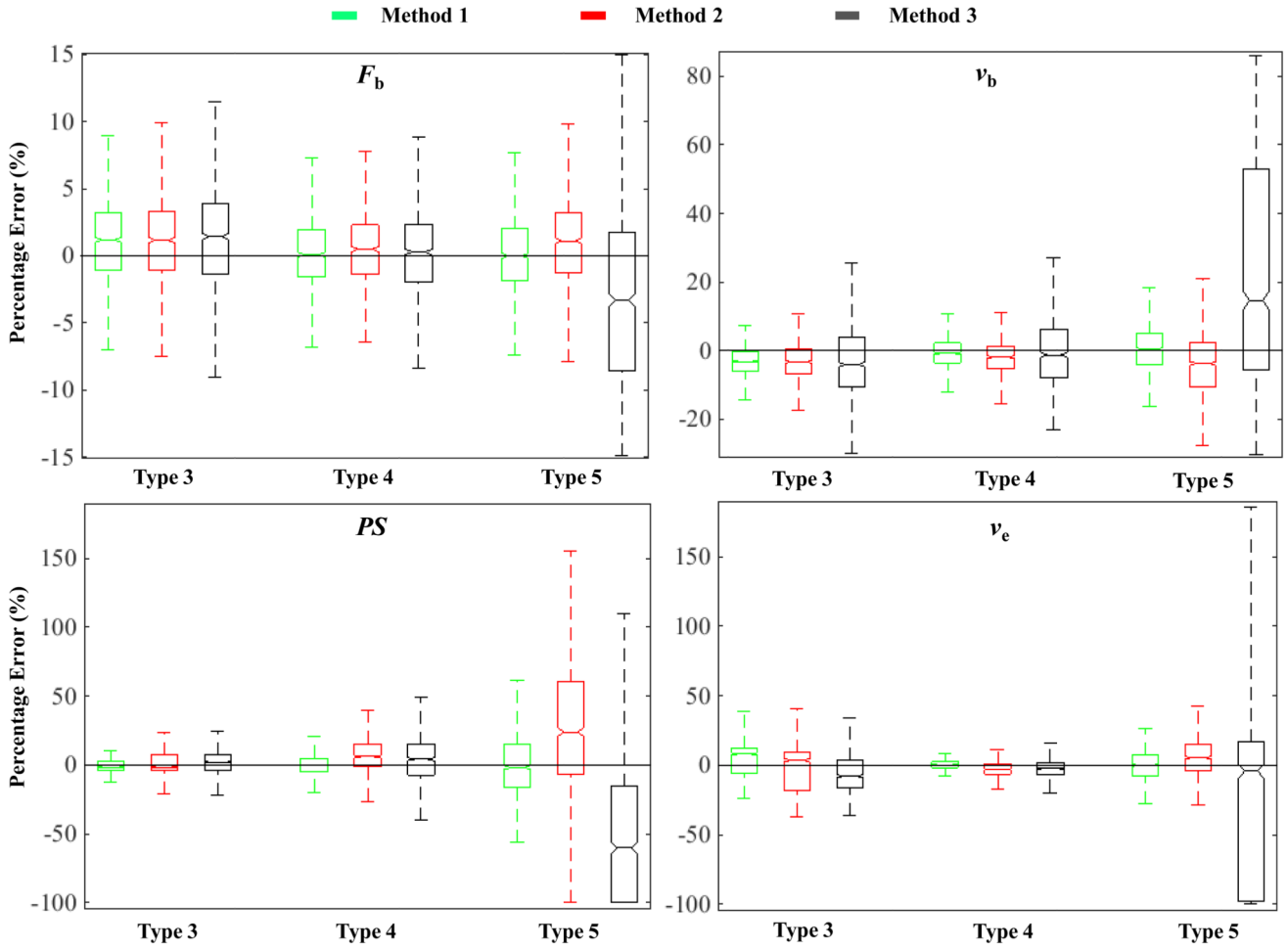

Figure 2.

Box and whisker plots of the simulation results for a signal to noise ratio (SNR) 50. Each parameter plot groups the results by curve type (3, 4 and 5) and sampling strategy, method 1 (green), method 2 (red) and method 3 (black). Note the variation in y-axis scale. The box represents the middle 50% of values for the group (inter-quartile range) and the upper and lower whiskers represent the complete range beyond the middle 50%.

Europe PMC Funders Author Manuscripts

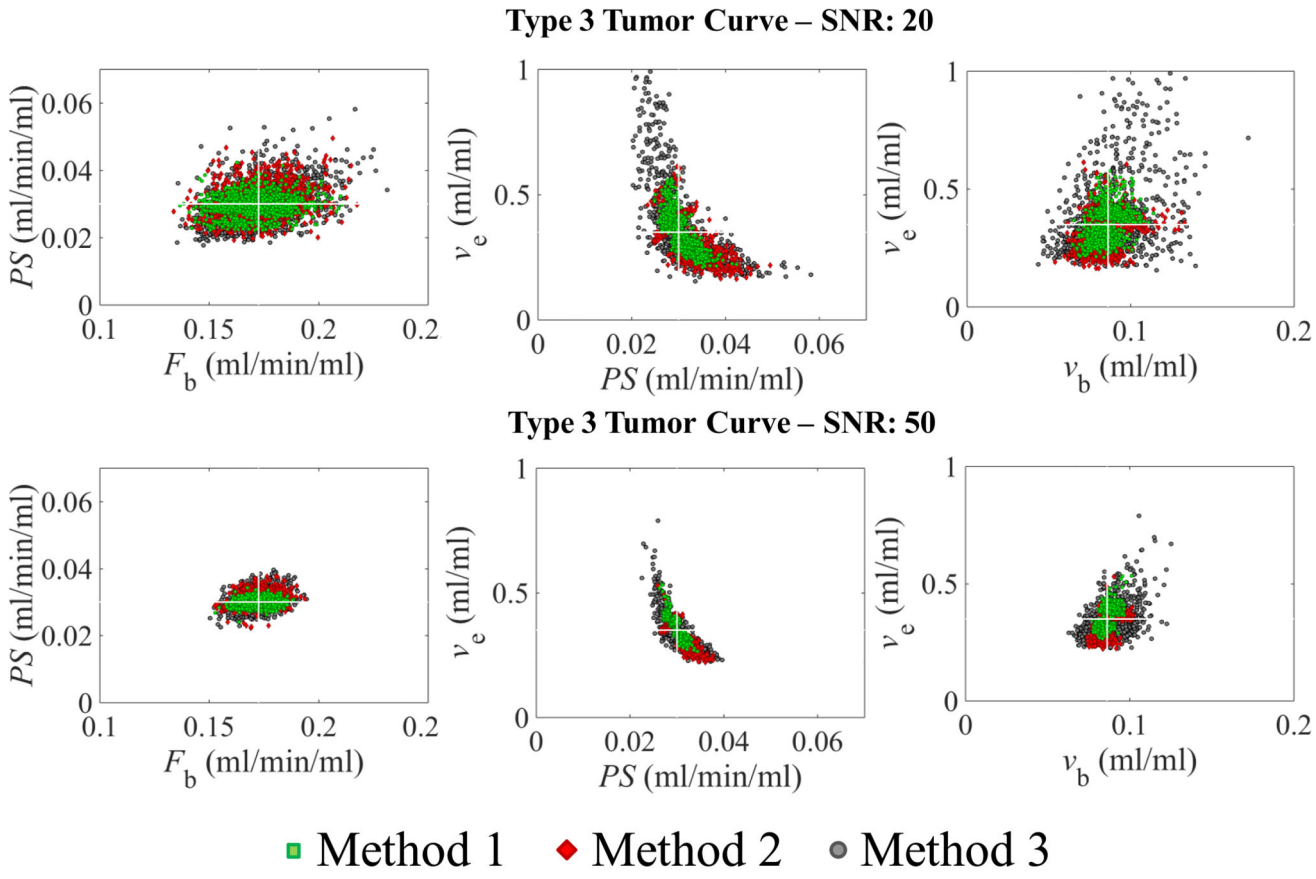

Figure 3.

Scatter plots of combinations of parameter estimates from the simulation of type 3 tumor curves and a signal to noise ratio (SNR) of 20 (top row) and 50 (bottom row). The middle panel (v_e vs PS plot) demonstrates that the optimization process generates imprecise v_e estimates, particularly for method 3 (grey circles). However, as the SNR increases the precision increases. Note that F_b, PS and v_b are estimated with a higher accuracy and precision than v_e. The white cross indicates the ground truth of the parameters.

Europe PMC Funders Author Manuscripts

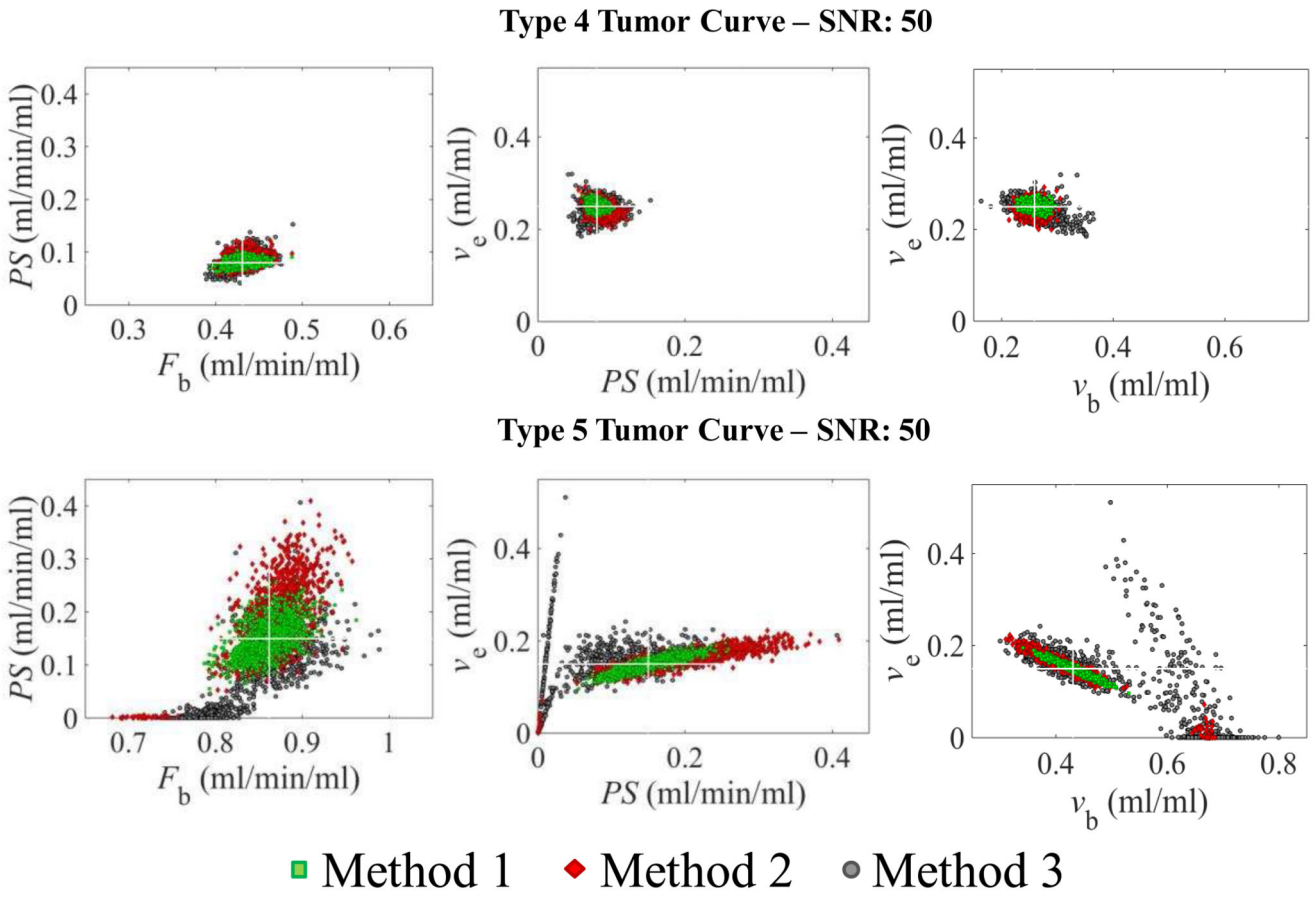

Figure 4.

Scatter plots of combinations of parameter estimates from the simulation of type 4 (top row) and type 5 tumor curves (bottom row) and a signal to noise ratio (SNR) of 50. The simulation results indicate that the performance of the optimization process is excellent for the type 4 curves for all methods. On the other hand, for type 5 curves PS estimates are imprecise and using method 3 (grey circles), the tracer kinetic model sometimes breaks down and returns PS estimates close to zero. This causes an overestimation of v_b, underestimation of F_b and a wide range of v_e estimates. The white cross indicates the ground truth of the parameters.

Europe PMC Funders Author Manuscripts

Europe PMC Funders Author Manuscripts

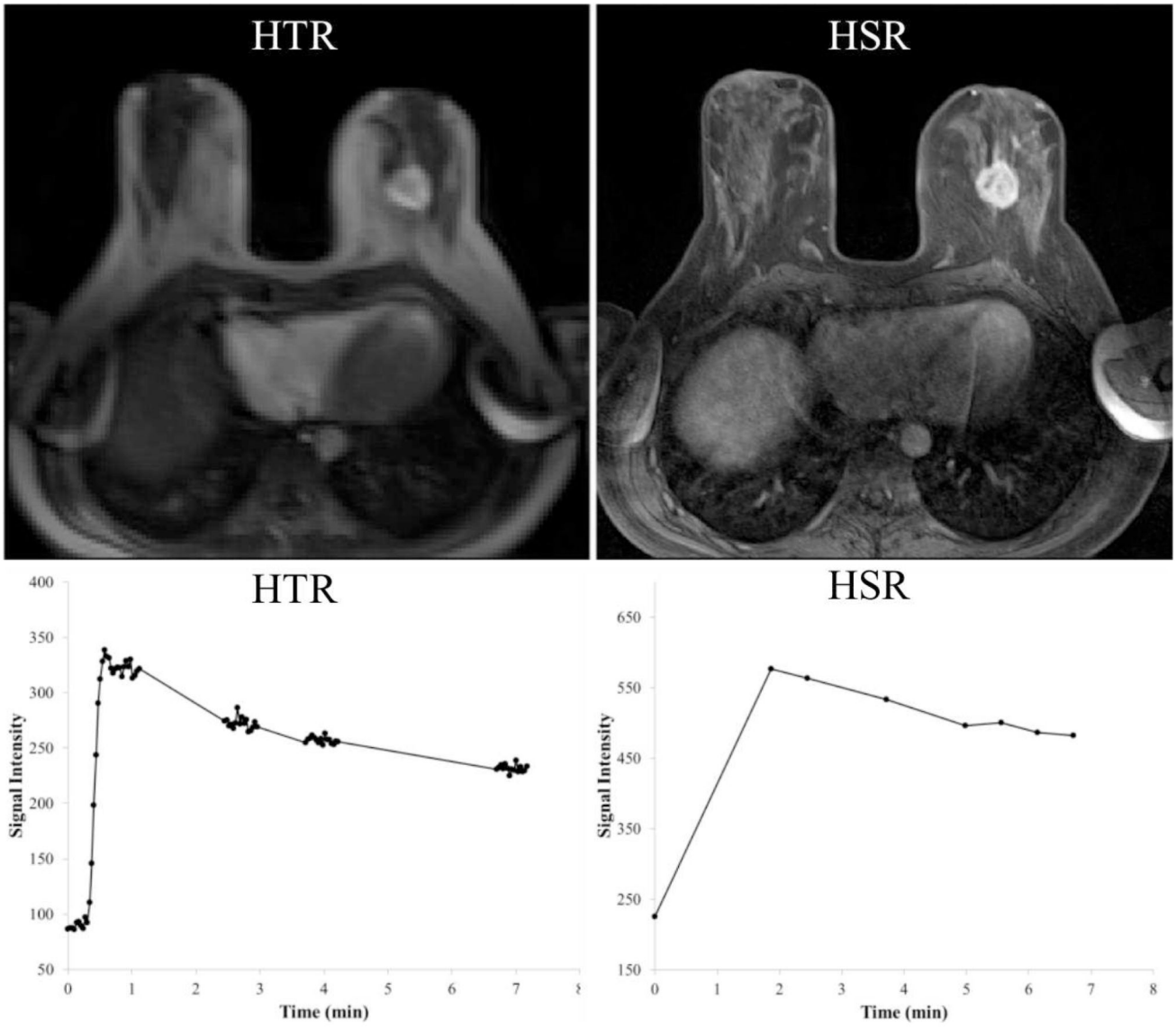

Figure 5.

High temporal resolution (HTR) 3D FLASH MR image during the first segment of HTR acquisitions in patient 12 (post-contrast), with the corresponding signal intensity time series from the tumor in the left breast. In the right column, high spatial resolution (HSR) 3D FLASH image acquired shortly after contrast agent administration with the respective signal time series. This figure illustrates the ability of the interleaved technique to preserve HSR images that can be used for clinical reporting. The tumor was reported as an abnormally enhancing 27 mm mass exhibiting a type 5 curve with 150% enhancement.

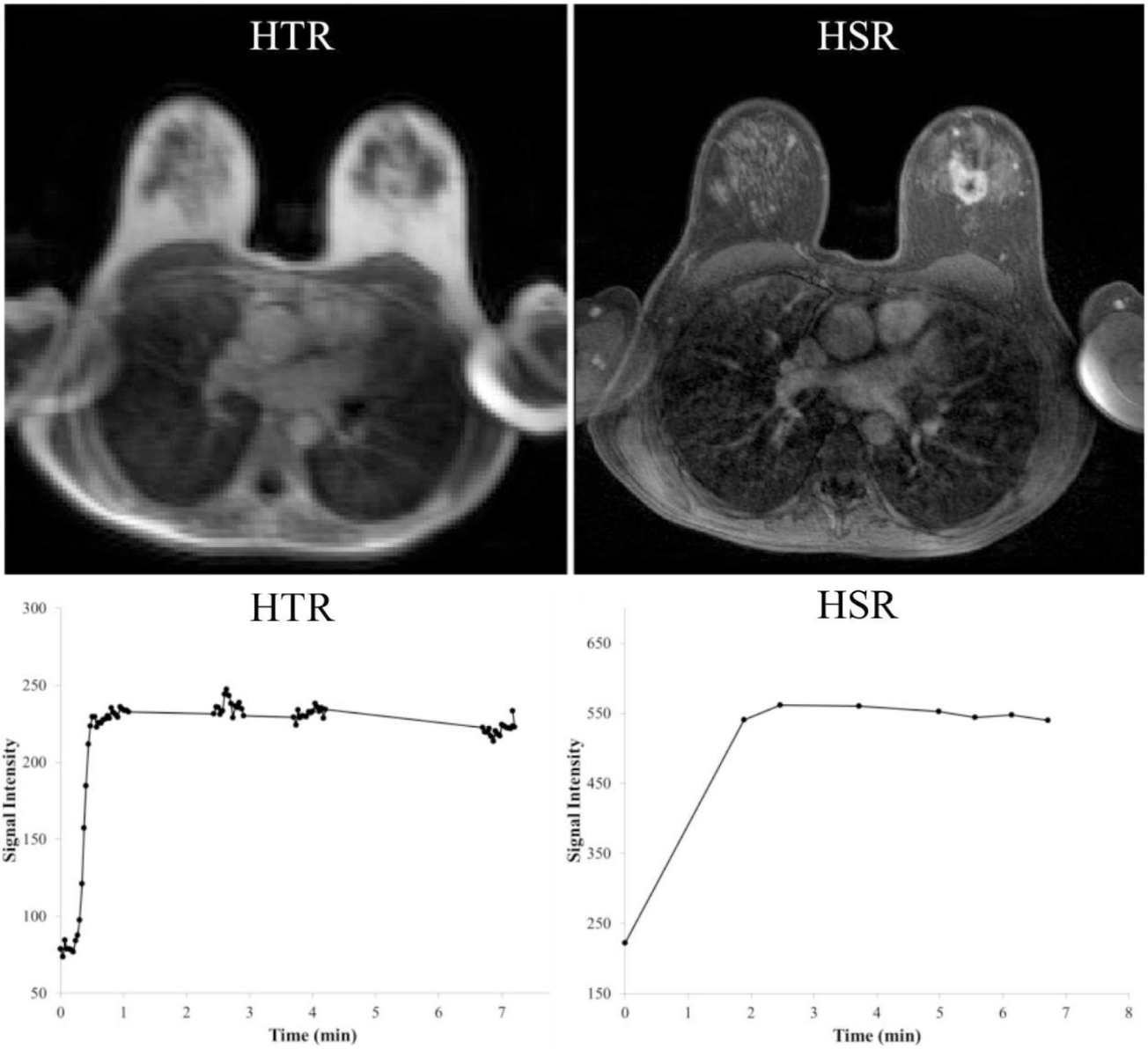

Figure 6.

High temporal resolution (HTR) 3D FLASH MR image during the first segment of HTR acquisitions in patient 3 (post-contrast), with the corresponding signal intensity time series from the tumor in the left breast. In the right column, high spatial resolution (HSR) 3D FLASH image acquired shortly after contrast agent administration with the respective signal time series. The time series generated from both the HSR and HTR images indicate a type 4 tumor curve. Also note that low enhancement areas within tumor can be identified on both HSR and HTR images. This tumor was reported as a large abnormal rim enhancing 45 mm mass exhibiting a type 4 curve with 120% enhancement.

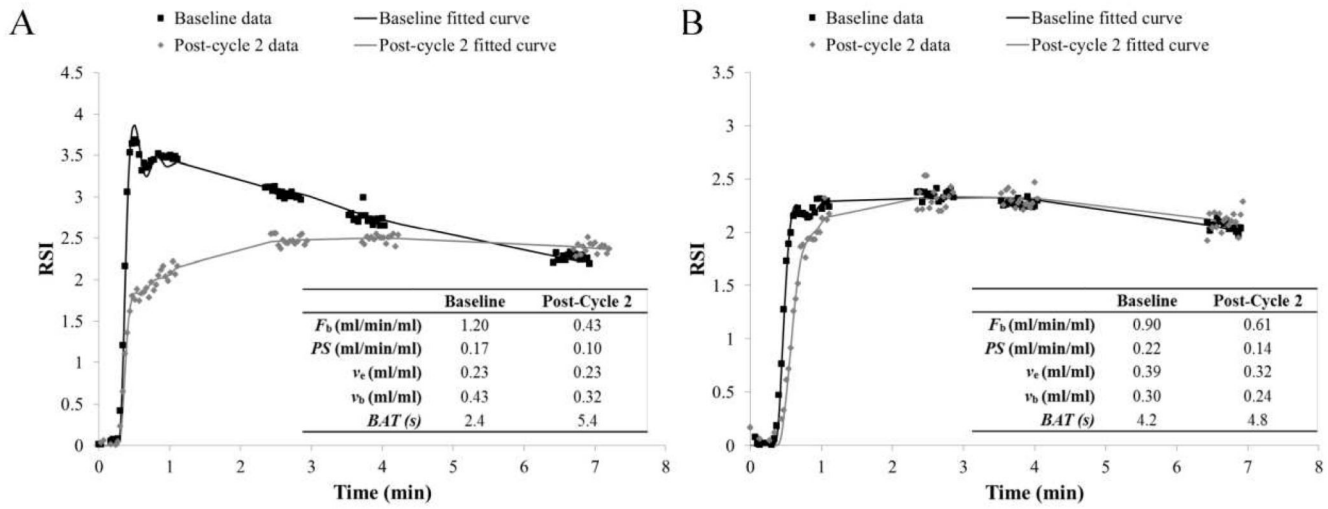

Figure 7.

MR data acquired at baseline and post-cycle 2 with respective fits and parameter estimates for patient 14 (A) who showed complete pathological response following 7 cycles of neoadjuvant chemotherapy (NACT) and patient 17 (B) who showed partial pathological response following 6 cycles of NACT.

Europe PMC Funders Author Manuscripts

Europe PMC Funders Author Manuscripts

Table 1

Parameters used in Simulations

	Tracer Kinetic Model Parameters				Physiological Parameters		
Tumor Curve	**F_b (ml/min/ml)**	**PS (ml/min/ml)**	**v_e (ml/ml)**	**v_b (ml/ml)**	**Blood $_{1,0}$ (ms)**	**Tumor $T_{1,0}$ (ms)**	**Hct**
Type 3	0.17	0.03	0.35	0.09			
Type 4	0.43	0.08	0.25	0.26	1400	1000	0.42
Type 5	0.86	0.15	0.15	0.43			

$T_{1,0}$: Precontrast longitudinal relaxation time, Hct: Hematocrit

Europe PMC Funders Author Manuscripts

Table 2
Patient Histological Data and chemotherapy regime

Patient No.	Age	Lymph nodes	Tumor Type	Grade	ER status	PR status	HER 2 Status	NACT Regime
1	58	-	Ductal NST	2,3	-	-	+	4×EC + 4×DC
3	40	+	Ductal NST	2	+	-	+	2×EC + 4×DC
4	47	-	Ductal NST	2	+	+	+	6×EC
5	40	+	Ductal NST	2	+	+	-	4×EC + 2×DC
6	49	+	Ductal/Lobular	1	+	+	-	2×EC + 6×DC
7	50	-	Ductal NST	3	-	-	-	4×EC + 4×DC
8	42	+	Ductal NST	2	+	+	-	3×DC + 3×FEC
9	47	+	Ductal NST	3	+	-	-	3×DC
10	50	-	Ductal NST	2	+	+	-	3×EC + 4×DC
11	61	+	Ductal NST	3	+	-	+	4×EC + 4×DC
12	42	+	Ductal NST	2	+	+	-	4×EC + 4×DC
13	45	+	Ductal NST	3	-	-	-	4×EC + 4×DC
14	54	+	Ductal NST	3	-	-	+	4×EC + 3×DC
15	61	+	Ductal NST	3	-	-	-	4×EC + 4×DC
16	60	+	Basal Features	3	-	-	-	4×EC + 4×DC
17	38	+	Ductal NST	2	+	-	+	2×EC + 4×DC
18	53	+	Ductal NST	2,3	+	-	-	3×EC + 4×DC
20	40	+	Ductal NST	3	+	-	-	4×EC + 2×DC

Ductal NST: ductal carcinoma of no specific type, ER: estrogen receptor, PR: progesterone receptor, HER 2: human epidermal growth factor receptor 2, EC: epirubicin & cyclophosphamide, DC: docetaxel & cisplatin, FEC: fluorouracil & EC.

Table 3

Values of Estimated Parameters

Parameters	Baseline MRI (n=15)	Paired Data		p-value
		Baseline MRI (n=10)	Post-Cycle 2 MRI (n=10)	
	Median (range)	Median (range)	Median (range)	
Volume (ml)	13.67 (0.61 - 108.37)	16.33 (2.32 - 108.37)	7.69 (0.19 - 68.47)	0.065
Tumor T_1 (ms)	1074 (948 - 1196)	1070 (948 - 1196)	1113 (962 - 1273)	0.432
Blood T_1 (ms)	1335 (1241 - 1489)	1324 (1241 - 1489)	1384 (1317 - 1560)	0.053
Hct	0.40 (0.35 – 0.46)	0.40 (0.37 – 0.46)	0.40 (0.28 - 0.47)	0.625
BAT (s)	3.60 (1.80 - 9.60)	3.60 (1.80 - 5.40)	4.80 (3.00 - 8.14)	0.020[a]
F_b (ml/min/ml)	0.68 (0.16 - 1.36)	0.81 (0.34 - 1.36)	0.43 (0.19 - 0.84)	0.002[a]
PS (ml/min/ml)	0.08 (0.01 - 0.37)	0.10 (0.05 - 0.37)	0.08 (0.05 - 0.15)	0.106
v_e (ml/ml)	0.22 (0.09 - 0.39)	0.26 (0.16 - 0.39)	0.25 (0.14 - 0.33)	0.625
v_b (ml/ml)	0.25 (0.01 - 0.59)	0.24 (0.04 - 0.49)	0.23 (0.07 - 0.45)	0.695
E (no units)	0.19 (0.02 - 0.44)	0.19 (0.11 - 0.44)	0.25 (0.11 - 0.46)	0.322
K^{trans} (/min)	0.06 (0.01 - 0.25)	0.09 (0.04 - 0.25)	0.06 (0.04 - 0.10)	0.037[a]

[a] A difference, at 95% significance level, using a non-parametric Wilcoxon signed rank test.

Median parameter estimates (range) for the tracer kinetic model, tumor volume and T_1 for tumor and blood ROIs. A non-parametric Wilcoxon signed rank test was used to compare the baseline and post-cycle 2 parameter estimates who attended both MRI sessions (paired data). Hct = Haematocrit, BAT = bolus arrival time, F_b = tumor blood flow, PS = permeability surface-area product, v_e = interstitial volume fraction, v_b = blood volume fraction, E = extraction fraction, K^{trans} = volume transfer constant.